Engineering Tertiary Chirality in Helical Biopolymers

Jordan Janowski[1†], Van A.B. Pham[2†], Simon Vecchioni[1†], Karol Woloszyn[1], Brandon Lu[1], Yijia Zou,[1] Betel Erkalo,[1] Lara Perren[1], Joe Rueb[1], Jesse Madnick[3], Chengde Mao[4], Masahico Saito[2], Yoel P. Ohayon[1], Nataša Jonoska[2*], Ruojie Sha[1*]

[1]Department of Chemistry, New York University, New York, NY 10003, USA
[2]Department of Mathematics and Statistics, University of South Florida, Tampa, FL 33620, USA
[3]Department of Mathematics, University of Oregon, Eugene, OR 97403, USA
[4]Department of Chemistry, Purdue University, West Lafayette, IN 47907, USA
[†]Contributed Equally
[*]Corresponding authors: R.S. (ruojie.sha@nyu.edu), N.J. (jonoska@mail.usf.edu)

Abstract

Tertiary chirality describes the handedness of supramolecular assemblies and relies not only on the primary and secondary structures of the building blocks, but also on topological driving forces that have been sparsely characterized. Helical biopolymers, especially DNA, have been extensively investigated as they possess intrinsic chirality that determines the optical, mechanical, and physical properties of the ensuing material. Here we employ the DNA tensegrity triangle as a model system to locate the tipping points in chirality inversion at the tertiary level by X-ray diffraction. We engineer tensegrity triangle crystals with incremental rotational steps between immobile junctions from 3 to 28 base pairs (bp). We construct a mathematical model that accurately predicts and explains the molecular configurations in both this work and previous studies. Our design framework is extendable to other supramolecular assemblies of helical biopolymers and can be used in the design of chiral nanomaterials, optically-active molecules, and mesoporous frameworks, all of which are of interest to physical, biological, and chemical nanoscience.

Significance

Macromolecules naturally fold into supramolecular assemblies to yield the complex topologies found in living biological systems. The rational design of synthetic molecular architectures has underscored chemical bioengineering for decades, while the development of structural DNA nanotechnology has yielded a variety of 3D molecular architectures and crystals with potential for multiple applications in material science, physics and engineering. Control over the geometric features of monomers informs the long-range order of the ensuing supramolecular lattices, yet current understandings of branched geometry have not been sufficient to predict and control the chirality of small, folded molecular shapes. Here we describe a generalizable method to predict and build chiral supramolecular assemblies from DNA. A thorough crystallographic library is constructed that validates our model, and at the same time we extract the key topological properties as driving forces for chiral self-assembly in helical biopolymers. Understanding the stimuli for different molecular chirality is of interest in biophysical studies, medical nanotechnologies, and the design of hierarchical nanomaterials.

Introduction

Chirality can be defined as the intrinsic handedness of molecules and molecular assemblies across scales. At the smallest dimension, chirality is pervasive in primary structure, where it describes the placement of chiral centers in predominantly ring-like species. At the macromolecular scale, chirality describes the handedness of quaternary assemblies of protein subunits, such as the ATP

synthase complex, whose chiral operation dictates the catabolism or anabolism of ATP in eukaryotes. Self-assembly of materials with predesigned chirality has been of intense interest to materials scientists at various levels of complexity, including solid state assemblies of nanoparticles, metal ions, and copolymer species.(1-5)

DNA has been used as a design language for the self-assembly of designer nanomaterials since the demonstration of the immobile Holliday junction in 1983.(6) The right-handed "J1" configuration has been extensively incorporated into 1D and 2D DNA motifs, from tile-based arrays to DNA origami, and possesses a natural crossing angle of 62.5°.(6-13) Exploiting the natural J1 angle to build a chiral triangular tile with intrinsic 60° angles, the tensegrity triangle was developed to self-assemble into macroscopic crystals via self-assembly.(14, 15) This 3D framework opened the door to a wide variety of solid-state devices based on crystalline biopolymers.(16-28)

The structure of an immobile junction isoform, the left-handed "L1" junction, which possesses the same sequence and stacking pattern as the J1 junction was recently reported in a 3D triangular tile.(29) Previous studies predicted the left-handed nature of such junctions,(30-32) which have been observed in RNA/DNA hybrids.(33) Subsequent molecular dynamics simulation showed that a left-handed junction conformation was topologically possible, but remained a short-lived state in the absence of a locking mechanism.(13) With this work we establish a range of DNA tensegrity triangles that leverage the J1 and L1 junctions as chiral building blocks to self-assemble into chiral supramolecular nanostructures. We develop a mathematical model from first principles to explain the observed handedness of helical motifs, and we demonstrate the experimental robustness of these findings.

Experimental Results

The DNA tensegrity triangle possesses an intrinsic tertiary handedness, owing to the over-under stacking of the double helices to form a triangular frame (**Fig. 1A,B**).(14, 15, 34) There exist many variations on this frame,(19) however throughout this study we employ equilateral, sequence-symmetric triangles composed of three DNA oligomers with the conserved J1/L1 sequence (GG/AC). A key "center strand" traverses around the triangle frame to return to its origin, locking the motif into a closed configuration, with handedness emerging from the number of bp between junctions (*n*), or the *inter-junction spacing*.(29) The center strands, upon virtual closure of the nick, exhibit specific topological properties (**Fig. 1B**) that depend on the chirality of the triangle. These motifs readily crystallize by self-assembly to allow structure determination by X-ray diffraction (**Fig. 1C,D, Fig. S1A-M**). To validate our chiral control method, triangles with two, three and four turns of DNA (21, 31, 41-42 bp) per edge were crystallized with *n* between 3-28 bp (see Supplemental Methods, **Table S1**). Structures of triangles with $n = 3,7$ and 8 have been described previously,(14, 16, 29, 35) and a 17 bp case was reported without the J1 sequence.(36) In all, we deposit 13 new structures with predesigned chirality. Diffraction statistics are available in **Table S2**.

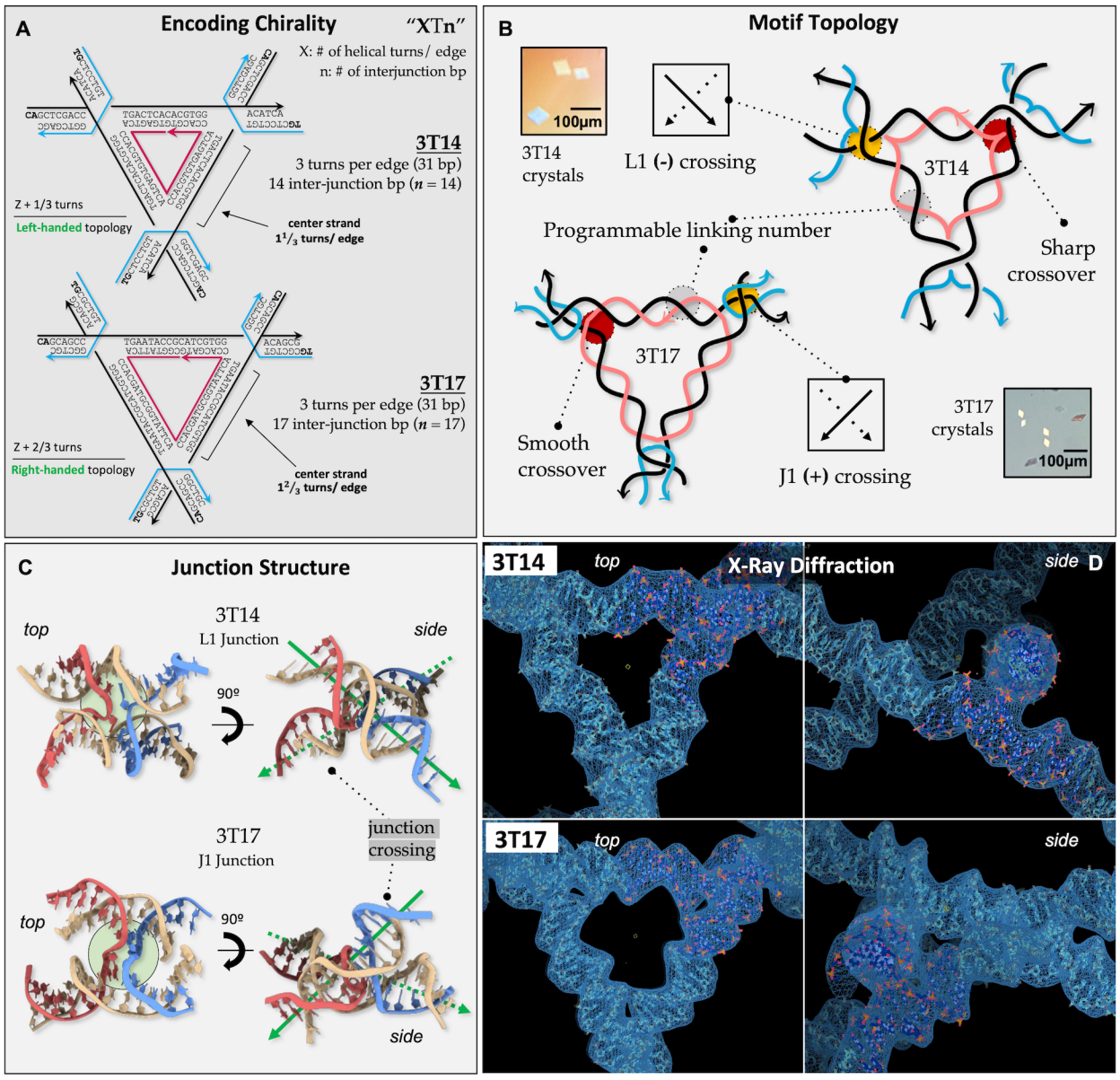

Figure 1: Engineering chirality in DNA triangles. **A)** Description of the design parameters of the tensegrity triangle. **B)** These motifs possess programmable topology and self-assemble into diffraction-quality crystals (inset). **C)** Structure determination by X-ray diffraction and the ensuing junction crossings are shown. D) $2F_o$-F_c electron density is shown for 3T14 and 3T17 from the top and side orientations.

Chiral control across size scales is apparent in **Fig. 2**, where two-, three- and four-turn DNA motifs are shown with the exemplary left- and right-handed motif at each level. Granular changes in inter-junction spacing for three-turn motifs are shown in **Fig. 3**, as well as two- and four-turn tiles in **Figs. S2-3**. Results are summarized in **Tables S3-5**. At each length scale, triangles with ~Z+1/3 (Z=0,1,2; for 3, 12, 13, 14, 24 bp) helical turns between junctions formed left-handed architectures, in accordance with previous predictions.(29, 31) In all cases, these left-handed, L1 junctions exhibit sharp corners at the crossover point where the right-handedness of the helix and the left-handedness of the junction clash (see **Fig. 2A-C**). Triangles with ~Z+2/3 (Z=0,1,2; for 7, 8, 16, 17, 18, 28 bp) helical turns formed right-handed architectures in a predictable manner. These right-

handed, J1 junctions possess smooth crossovers in looping curves that align with the natural twist direction of the helix (**Fig. 2D-F**). The center strand ribbon topology is shown in **Fig. 2I**, with the sharp, wrinkled L1 structures juxtaposed with the smooth, wavelike J1 motifs. Summing the number of times the center strand winds around the helical strand (depicted as line) of each side across the triangle yields a linking number calculation of the ribbon that is mathematically verified below.

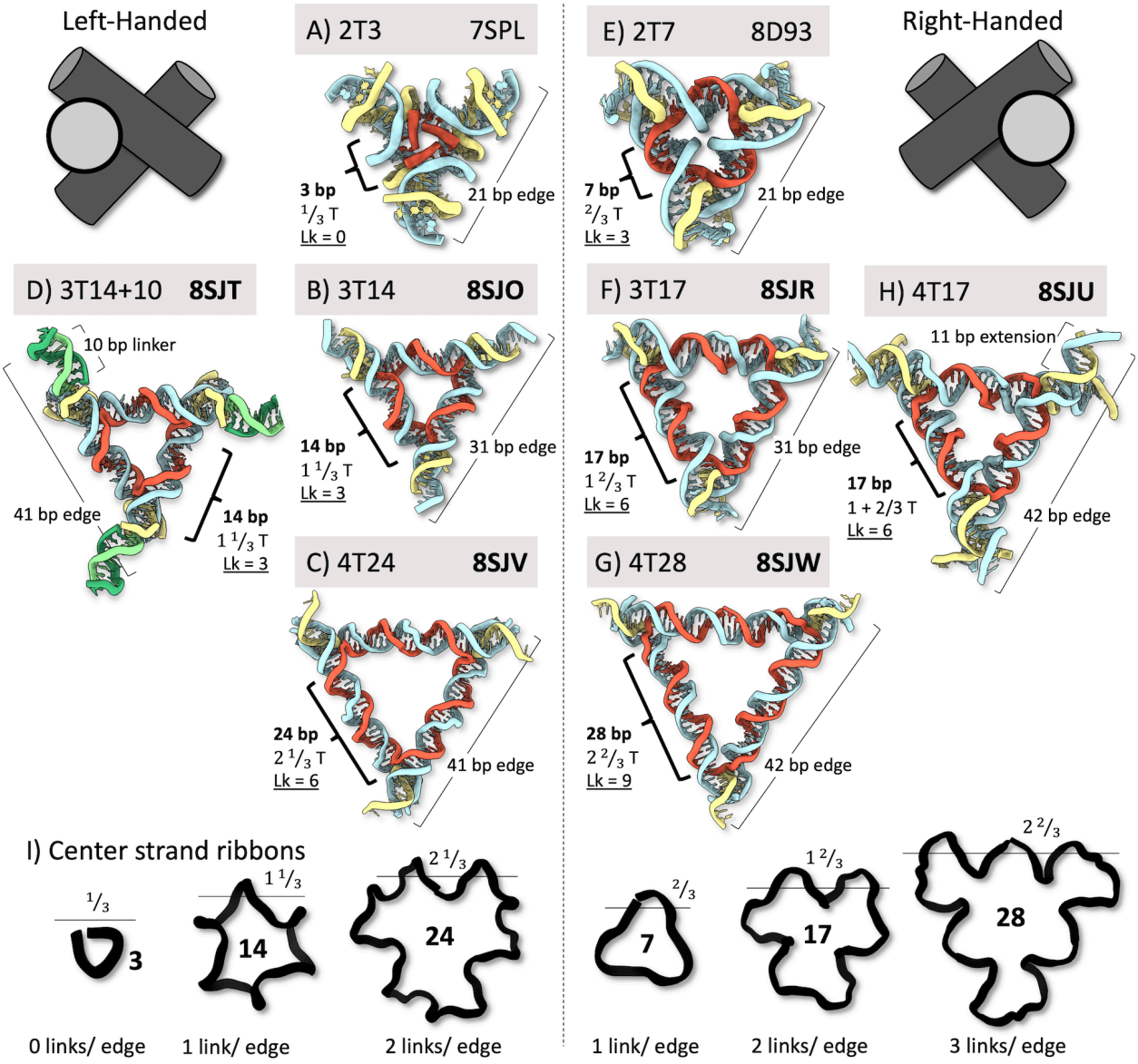

Figure 2: Structures of 2,3,4-turn triangles by X-ray diffraction, with left- and right-handed motifs and linking numbers (Lk); PDB ID's noted, bold for new depositions. **A-C)** Left-handed triangles possess Z+1/3 helical turns between junctions (Z = 0,1,2). **D)** 3T14 is augmented to carry a 10 bp linker to generate a four-turn analog (3T17+10). **E-G)** Right-handed topology arises with Z+2/3 helical turns (Z = 0,1,2). **H)** 3T17 is extended by 11 bp to generate a four-turn analog (4T17). **I)** Center strand ribbons are plotted to scale, showing the sharp corners of the left-handed family and the smooth edges of the right-handed family.

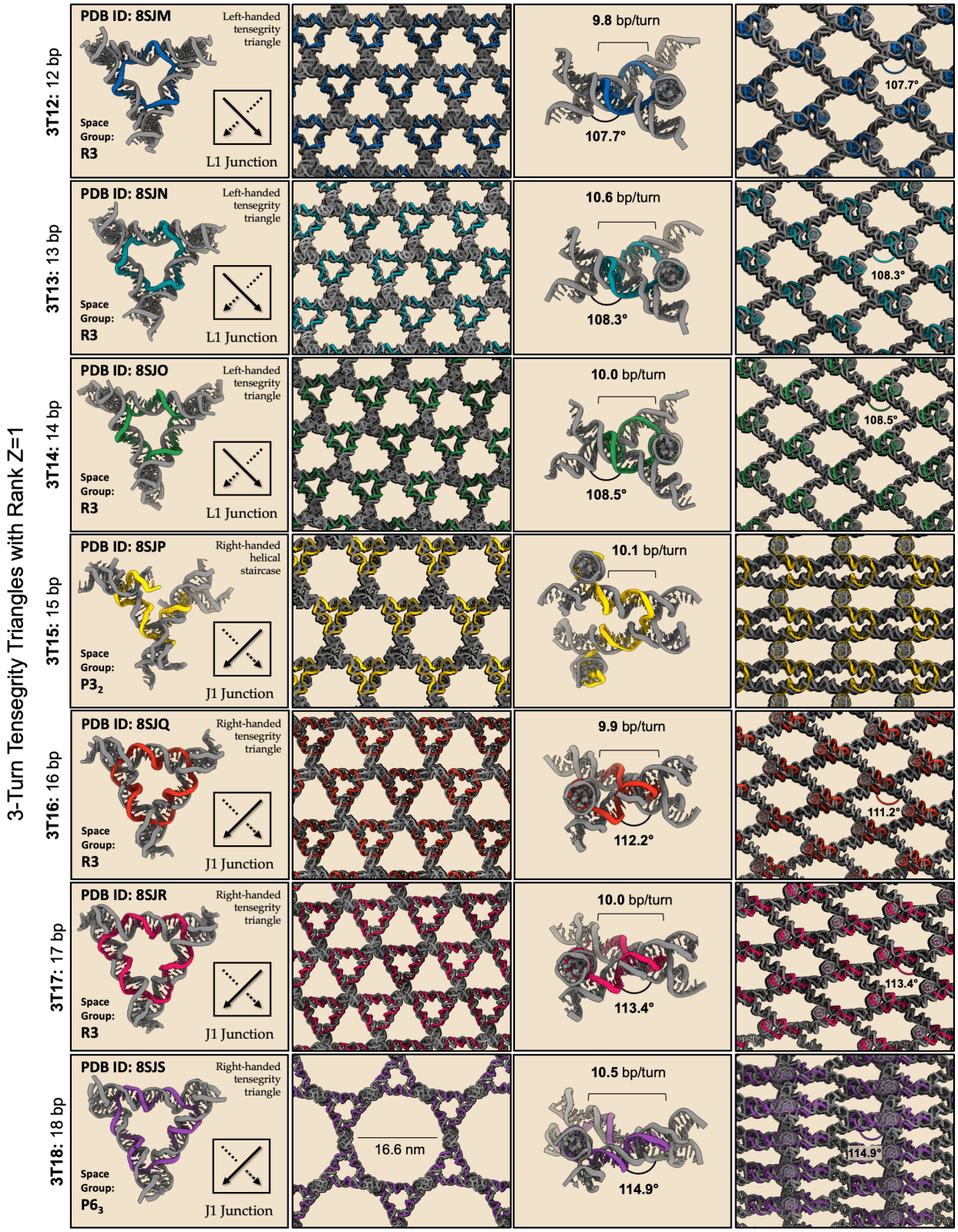

Figure 3: Structural library of three-turn tensegrity triangles of rank Z=1, 3T12-3T18. For each motif, the triangle structures are shown with center strands colored. Helicity, space group, junction type and crystallographic angle are shown, where relevant. Crystal lattices are shown down the three-fold axis as

well as along the helical axis. The 3T12, 3T13 and 3T14 motifs are left-handed triangles; 3T15 exhibits a right-handed, open, helical staircase; and the 3T16, 3T17 and 3T18 motifs are right-handed triangles.

We next sought to augment these motifs using arm extensions in a method described previously, which has been used for bandgap modulation in tensegrity architectures.(19, 28) We extended the extra-junction region of three-turn, 31 bp motifs by both 10 and 11 bp through chain lengthening or sicky-ended linkers (**Fig. 2D,H**). Right-handed augmentations were more robust with 11 bp covalent extensions to yield 42 total bp and exactly four turns of DNA, while left-handed augmentations were far better with 10 bp extensions and 41 total base pairs. This insight enabled the design and crystallization of four-turn triangles of 24 and 28 inter-junction bp with 41 and 42 bp edges, respectively (**Fig. 2C,G**). No four-turn left-handed triangle formed with 42 bp edges, indicating that the L1 junction exerts a torsional strain on the extra-junction region of tensegrity triangles.

All triangles described above form in the designed space group, R3. However, we observe that right handed-triangles at the upper limit of each rank (n = 8,18) exhibit torsional stress to cause a bend in the junction and sticky end to yield crystals with a hexagonal morphology in space group $P6_3$ (**Fig. 3**: 3T18). This effect has been observed previously by inducing under-twisting in triangle centers,(16, 17) and can be rescued by adding an extra base pair in the extra-junction region to relieve strain (see n = 18 bp with 32 bp edges in Zheng et al(14)). The inter-junction helicity of all motifs was between 9.8-10.6 bp/turn, with a relaxed, inter-junction standard of 10.1 bp/turn (**Tables S3-5**). By contrast, hexagonal assemblies were strained, with 10.5 bp/turn—near the observed limit. Furthermore, increasing n contributes to the overall flatness, or reduced tilt, of the triangles. The crystallographic rhombohedral angle (α) increases with the addition of each additional base pair from 79.0° with n = 3 bp to an apparent plateau at 115.3° and 115.1° with n = 24 and 28 bp, respectively (**Fig. 3**, **Figs. S2-3**). In these structures, bending is observed in the extra-junction region (**Fig. S3**).

Not all designs produced triangles. Motifs with ~Z helical turns between junctions (Z=1,2; for n=9,10,11,19 bp) yielded spherulites or did not crystallize. Motifs with ~Z+1/2 helical turns (Z=0,1; for n=5,6,15 bp) formed open, trigonal structures in space group $P3_2$ similar to those reported by Simmons (**Figs. 3**,**S2**).(21) A comprehensive study by that group using fourfold center strand symmetry yielded crystal lattices in the higher symmetry group $P3_221$ for n = 5,(37) while both the 5 and 6 bp motifs described here diffracted into $P3_2$. As such, we attribute the higher symmetry observed by Simmons and colleagues to the extra duplex copy in their "4x5" motif that folds into the crystal cavity to yield a nested lattice. We note that the authors were able to obtain $P3_2$ symmetry for n = 5 by changing the junction sequence (so called J3, J6, etc.), highlighting the effect of local stacking geometry and suggesting a course of study on L1 junction sequences (L2, L3, etc.). The three-turn Z+1/2 motif with 15 inter-junction pairs is highlighted in **Fig. 3**, as well as **Fig. S1F**. An apparently triangle-like view can be seen down the threefold axis, but rotation of the unit cell clearly shows that these helical cylinders lie on the crystallographic screw axis and do not form a topologically-closed shape.

Our experimental results underscore the effect of overall geometry by way of helical torsion and tilt on the chirality and topology of DNA motifs. In apparent violation of the other observed data,(29) the motif with n = 4 bp did not form crystals. This result, together with failed or trigonal lattices begs the question of *why* DNA motifs crystallize in the forms that they do.

Engineering Chirality—A Mathematical Model

Our mathematical model uses the center strand configuration to characterize the chirality of a unit tensegrity triangle structure. The model provides a framework that generates an array of possible center strand configurations and subsequently identifies the tensegrity triangle phenotypes that may form experimentally and ultimately become units in a crystal structure. Moreover, we compute topological and geometric properties of the center strands such as the local twist, writhe, and linking number for the experimentally observed structures (see **Fig. 4**).

For modeling purposes, the center strand of a closed triangular structure is considered as a circularly-ligated DNA strand. A previous study employed circularly-ligated center strands to yield crystals isomorphic to unligated ones,(38) demonstrating that the inevitable nick in a linear, symmetric oligomer does not greatly alter the physical properties of a center strand and its ensuing motif. Thus, the center strand consists of $3n$ nucleotides and defines the inter-junction region of the tensegrity triangle by three equal helical curve segments C_1, C_2, C_3, each of which represents a DNA backbone segment modeled on a cylinder of radius 1 nm (details included in Appendix A). The complementary strands are helical curves that lie on the same cylinders with opposite polarity. Possible configurations of the center strand $C_1C_2C_3$ are obtained by incrementing rotations of curves C_1, C_2 and C_3 by angle η about the curves' end points, denoted R_η. For each rotation, we compute the following properties:

- Smoothness at junctions, J, between the starting point of C_1 and ending point of C_3 is defined as the norm of the cross product of the unit tangent vectors at these curves. The smoothness is maximal for the minimal values of J. **Fig. 1B** illustrates the changes in smoothness between left- and right-handed structures.
- The internal triangle cavity distance, D, in nanometers, from the center of $C_1C_2C_3$ to respective cylinder sides.
- Tilt level, T, is the difference in nanometers of the terminal points of cylinder center line. $|T|$ must be greater than the diameter of the cylinder to have a non-flat tensegrity triangle construct. For $T > 0$ the resulting triangle is right-handed, and for $T < 0$ it is left-handed.

We assert that the preferred experimental configuration must appear in one of the η values when the central strand configuration obtains (i) the maximum tilt amplitude, $|T|$ is realized; (ii) the smoothness J at junctions must be a local extreme, either smoothest or sharpest; (iii) the triangle cavity D is maximized. For an η value satisfying these conditions we also compute

- Complementary strands clash d_c as a minimal distance between the complementary strands.

Therefore, in addition to the three conditions above, in the experimental construction of the tensegrity triangle motif it must be that (iv) the complementary (dashed) strands do not sterically clash.

Experimentally, left-handed triangles are characterized by center strands with sharp corners (locally maximal J) with the smallest (and negative) value of T; right-handed structures by smooth corners (locally minimal J) and the largest (positive) T, indicating that our model accurately

predicts tertiary chirality. Furthermore, the model explains why in certain cases the triangular structure does not form; that is, cases in which either the structure is open (n = 5,15 bp, etc.) or a crystal cannot form (n = 4,11 bp, etc.). For instance, for n = 4 bp (see **Appendix Fig. A7 and Table A2**), no rotation angle η yields $D > 0$ nm, indicating that in all configurations the center strand does not produce a cavity.

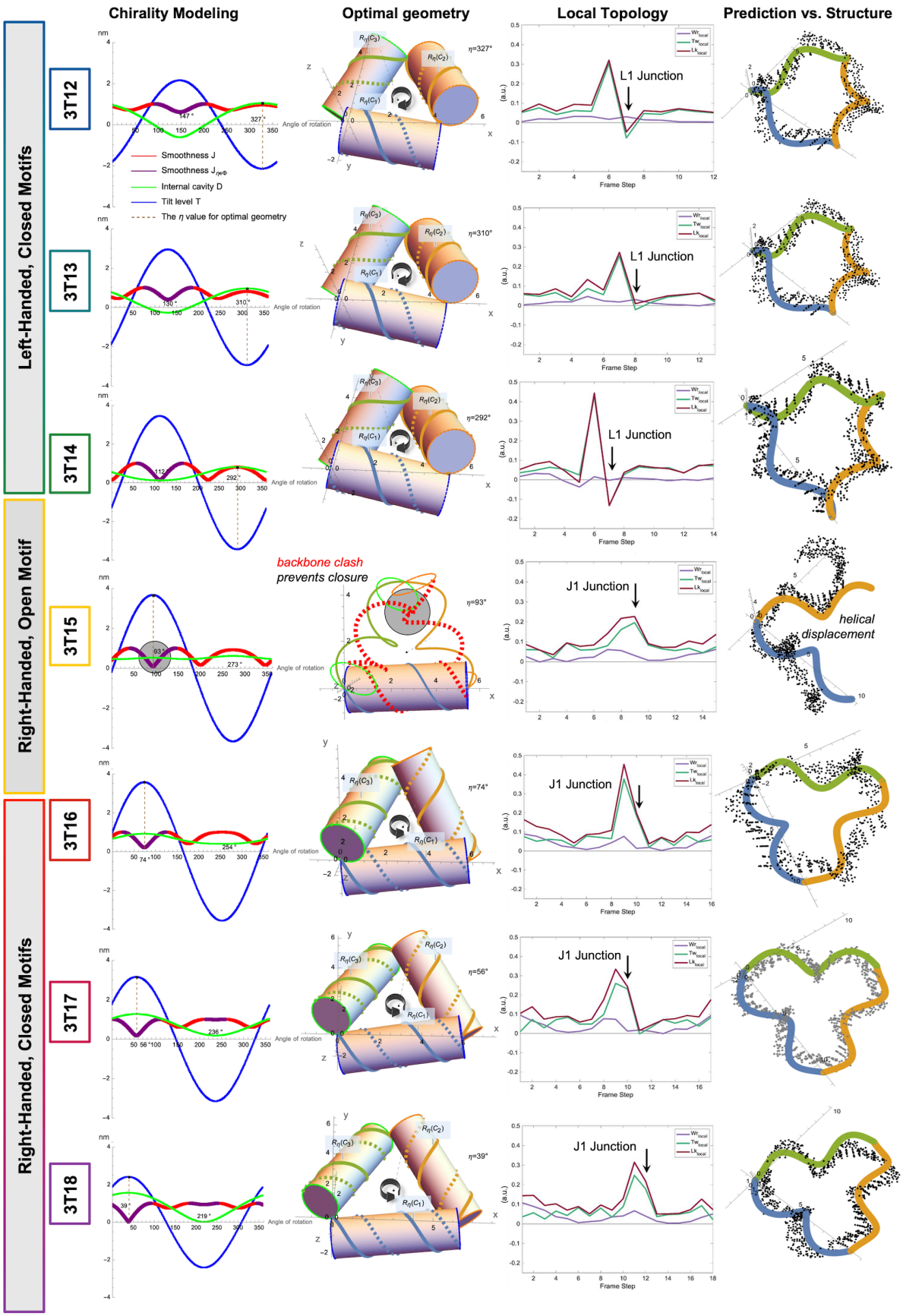
Chirality Modeling
Optimal geometry
Local Topology
Prediction vs. Structure
Left-Handed, Closed Motifs
Right-Handed, Open Motif
Right-Handed, Closed Motifs
3T12
3T13
3T14
3T15
3T16
3T17
3T18
Smoothness J
Smoothness J
Internal cavity D
Tilt level T
The η value for optimal geometry
Angle of rotation
Frame Step
L1 Junction
J1 Junction
backbone clash
prevents closure
helical
displacement

Figure 4: Geometric optimization, topological analysis, and comparison of model and experimental data. Column one exhibits optimization criteria: tilt level, *T* (blue); sharpness, *J* (red); smooth connections in center strand (purple); internal cavity, *D* (green). Column two shows optimized geometry. In the case of *n* = 15, the optimal model suggests that a closed triangular structure would be impractical because of clashing (dashed) strands. To alleviate this clash, the triangle opens to form a trigonal, right-handed lattice. The third column shows geometric parameters from the crystal structure integrated across the center strand of the asymmetric unit: local linking, Lk (red), local twist, Tw (green); and local writhe, Wr (purple). The final column shows an overlay of the predicted center strand geometry and the crystal structure. We note the handedness changes on the second column with the blue cylinder along the x-axis switching from being under (left-handed) to over (right-handed) the orange cylinder (see **Fig. 1B**). We indicate this through a handedness arrow at the center of each cylinder model.

It is well known that the linking number (Lk) of two non-intersecting curves can be written as the sum of the writhe (Wr) and twist (Tw) of the ribbon connecting those curves (see Appendix B). Considering the center strand as a ribbon, a curious discrepancy arises—a right-handed triangle with 5/3 turns per edge should yield $3*(5/3) = 5$ links, but has an apparent linking number of 6; while a left-handed triangle with 4/3 turns between junctions should have $3*(4/3) = 4$ links, but has an apparent linking number of 3 (**Fig. 2I**). To understand how the handedness of junctions affects the linking invariant, we carried out a geometric analysis of the center strands to quantify and explain this effect.(39-41) Full topological analysis can be found in the Supplemental Information in **Figs S4-S6**, **Tables S3-S5**, and Appendix B, but we summarize these findings in **Fig. 5**.

Plotting the Gauss linking integral (formula 3.1, Appendix B) of triangle center strands highlights bp steps that generate local linking extrema (**Fig. 4** column 3, **Fig. 5C-H, Figs. S4-S6**), which unsurprisingly correspond with the junction steps. We find that all triangles, irrespective of chirality, possess a positive one-third link between the junction step and the preceding bp step as a result of the 120° turn imposed by the triangle frame ($Lk_{rot} = 0.27 \pm 0.08$)(**Fig. 5I,J**). At the junction step itself, all left-handed triangles possess a strong negative self-link as a result of the right-handed DNA molecule making a sharp left turn ($Lk_{L1} = -0.12 \pm 0.04$) (**Fig. 5K**). By contrast, all right-handed motifs exhibit a strong positive link as a result of the right-handed helix making a right-handed crossover ($Lk_{J1} = 0.14 \pm 0.03$) (**Fig. 5L**). In this way, the difference between L1 and J1 linking is nearly 1/3 per junction.

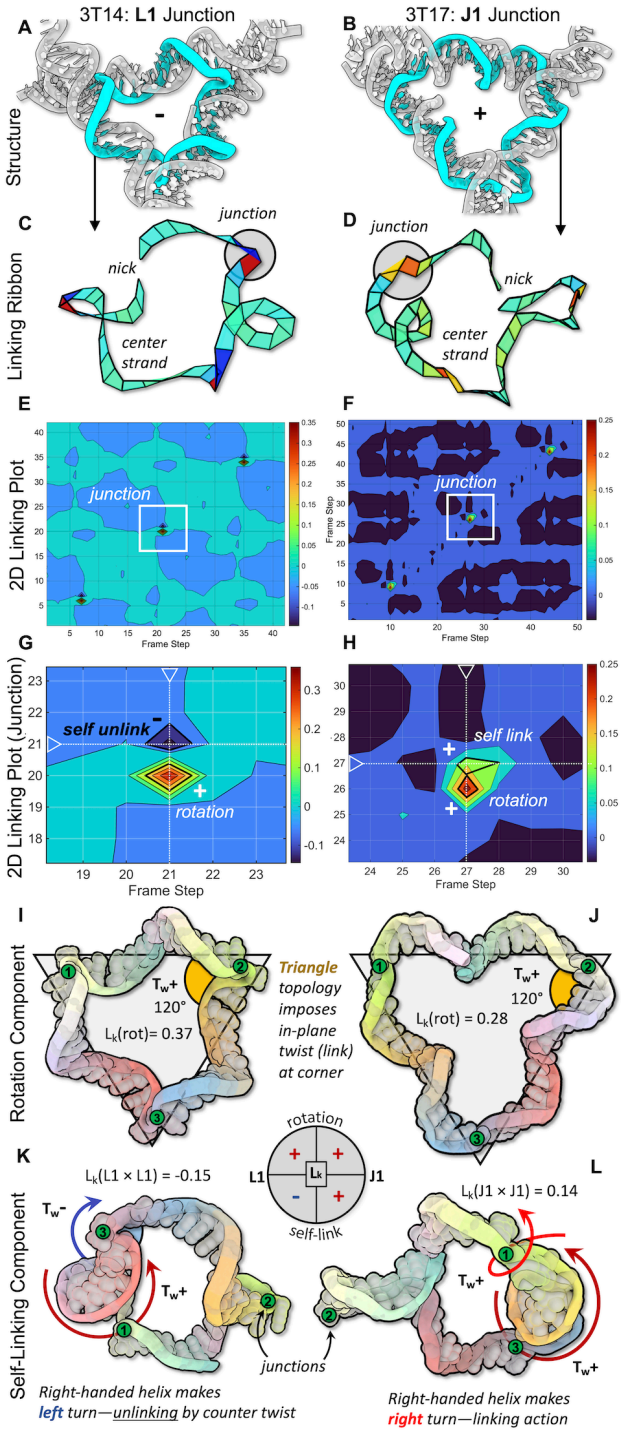

Figure 5: Linking topology of left- and right-handed DNA triangles, 3T14 and 3T17. **A-B)** The triangle center strands (cyan) are **C-D)** converted into a discrete ribbon. Plot of Gauss linking integrals were calculated and plotted onto the surface (See Appendix B, formula 3.1). **E-F)** Heat maps of the integration bins across the whole ribbon are generated, and base pair steps corresponding to junctions are boxed. **G)** White crosshairs indicate the negative self-link at the junction for 3T14 (step 21) and **H)** the positive self-link in 3T17 (step 27). Both triangles exhibit a positive link at the *junction-adjacent* position. **I-J)** All triangles studied here include a positive 1/3 link at the junction step from the triangle frame. **K)** By contrast, the twist contribution of a left-handed junction in a right-handed helix is negative, generating roughly -1/6 link per junction (Lk(L1) = -0.15), while **L)** a right-handed crossover in a right-handed helix generates a positive 1/6 link (Lk(J1) = 0.15).

Conclusion

In this study, we have carried out a systematic crystallographic study of tertiary chirality in DNA triangles, finding that motifs with inter-junction spacings between 3 bp (1/3 helical turns) and 28 bp (2+2/3 helical turns) agree with the Rule of Thirds where Z+1/3 and Z+2/3 helical turns between junctions yield left- and right-handed triangles, respectively.(29) To understand the mechanism of action in this system, we built a mathematical model that extracts and predicts the topological and geometric drivers of tertiary chirality. We find that the inter-helical tilt (T), crossover smoothness (J) and internal cavity (D) predict the chirality of a given helical assembly, and combined with the complementary strand distance (d_c) describes the ability of this motif to close into a trigonal assembly. Furthermore, we find that left-handed crossings possess a quantifiably negative self-link, while right-handed junctions are positively self-linked throughout the crossover region. Through geometric analysis, we have identified both a working description of *why* DNA triangles form with a preferred tertiary chirality, and further *how* this topology is manifest on a nucleotidyl level.

We anticipate that future modulation of the motifs in this study may elucidate the geometric effects from counter ions, small molecules, torsion and supercoiling on supramolecular chirality. Our results have implications for biological systems, wherein DNA crossovers are the drivers of information exchange during meiosis. An understanding of the topological effects on the handedness and geometry of the immobile junctions studied here will inform the study of mobile Holliday junctions and provide insight into the exchange mechanisms that arise in genetic recombination. Indeed, multiple crossover units have been observed in physiological systems: the double crossover (DX) has been identified as an intermediate in the repair of double stranded breaks in meiotic recombination;(42) while paranemic crossovers (PX), another interlocked Holliday junction species,(43) has been identified in the homology recognition process during meiotic synapsis and repeat-induced point mutation.(44, 45) PX molecules have also been identified in supercoiled plasmids containing homologous segments,(46) were shown to bind specifically to DNA polymerase I,(47) and are capable of being cloned *in vivo*.(48) The closed DNA motifs described here will enable studies on the activity of topoisomerases and junction resolvases when presented with precisely prescribed topology, chirality and helical torsion in "stacked-X" Holliday junction conformers. We expect biophysical studies to elucidate the topological entropy and folding kinetics of such systems, and we further envision mathematical studies which develop tools to describe the interplay between local tile geometry and global crystal symmetry. Functionalization of these architectures with nanoparticle or dye molecules will enable materials development for light harvesting, plasmonic waveguides, or photonic crystal design—applications where the supramolecular chirality has directly measurable optical or physical effects.

Finally, our mathematical model is derived from first principles and is therefore composable. By altering the input parameters of helical period, radius, and topology, it can be extended to describe supramolecular assemblies of other nucleic acids (RNA, PNA, etc.) and peptide helices. We anticipate the use of these methods to build chiral tiles built from other helical polymers to expand the design lexicon of self-assembling nanosystems.

Acknowledgements
We acknowledge support of grants N000141912596 from the Office of Naval Research to R.S., DE-SC0007991 from the Department of Energy to R.S., CCF-2106790 from the National Science Foundation to R.S., CCF-2107393 to C.M, and CCF-2107267 to N.J. We thank Professor James W. Canary of NYU for discussion and support throughout manuscript writing. We dedicate this work to the late Ned Seeman, who was a guiding light in the field of DNA nanotechnology.

Data Availability
Molecular structures were deposited to the Protein Databank under accession codes: 8SJM, 8SJN, 8SJO, 8SJP, 8SJQ, 8SJR, 8SJS, 8SJT, 8SJU, 8SJV, 8SJW, 8SL5, 8SZ5. Code and associated models are available at https://knot.math.usf.edu/software/. Additional data are available upon reasonable request to ruojie.sha@nyu.edu and jonoska@mail.usf.edu.

References

1. Y. Bi *et al.,* Controlled Hierarchical Self-Assembly of Nanoparticles and Chiral Molecules into Tubular Nanocomposites. *J. Am. Chem. Soc.* **145,** 8529-8539 (2023).

2. H.-F. Wang *et al.*, Networks with controlled chirality via self-assembly of chiral triblock terpolymers. *Science Adv.* **6**, eabc3644 (2020).
3. P. Kumar *et al.*, Photonically active bowtie nanoassemblies with chirality continuum. *Nature* **615**, 418-424 (2023).
4. H. Liu, A. E. Vladár, P.-P. Wang, M. Ouyang, Tuning Geometric Chirality in Metallic and Hybrid Nanostructures by Controlled Nanoscale Crystal Symmetry Breaking. *J. Am. Chem. Soc.* **145**, 7495-7503 (2023).
5. Y. Hu *et al.*, Single crystals of mechanically entwined helical covalent polymers. *Nature Chem.* **13**, 660-665 (2021).
6. N. R. Kallenbach, R.-I. Ma, N. C. Seeman, An immobile nucleic acid junction constructed from oligonucleotides. *Nature* **305**, 829-831 (1983).
7. E. Winfree, F. R. Liu, L. A. Wenzler, N. C. Seeman, Design and self-assembly of two-dimensional DNA crystals. *Nature* **394**, 539-544 (1998).
8. P. W. Rothemund, Folding DNA to create nanoscale shapes and patterns. *Nature* **440**, 297-302 (2006).
9. Y. He, Y. Tian, A. E. Ribbe, C. Mao, Highly connected two-dimensional crystals of DNA six-point-stars. *J. Am. Chem. Soc.* **128**, 15978-15979 (2006).
10. M. Kim *et al.*, Harnessing a paper-folding mechanism for reconfigurable DNA origami. *Nature* **619**, 78-86 (2023).
11. C. D. Mao, W. Q. Sun, N. C. Seeman, Designed two-dimensional DNA Holliday junction arrays visualized by atomic force microscopy. *J. Am. Chem. Soc.* **121**, 5437-5443 (1999).
12. W. Wang *et al.*, Reconfigurable Two-Dimensional DNA Lattices: Static and Dynamic Angle Control. *Angew. Chem. Intl. Ed.*, **60**, 25985-25990 (2021).
13. Z. Zhang *et al.*, Atomistic Picture of Opening–Closing Dynamics of DNA Holliday Junction Obtained by Molecular Simulations. *J. Chem. Info. Model.* **63**, 2794-2809 (2023).
14. J. Zheng *et al.*, From molecular to macroscopic via the rational design of a self-assembled 3D DNA crystal. *Nature* **461**, 74 (2009).
15. D. Liu, M. Wang, Z. Deng, R. Walulu, C. Mao, Tensegrity: construction of rigid DNA triangles with flexible four-arm DNA junctions. *J. Am. Chem. Soc.* **126**, 2324-2325 (2004).
16. B. Lu *et al.*, Programmable 3D Hexagonal Geometry of DNA Tensegrity Triangles. *Angew. Chem. Intl. Ed.* **62**, e202213451 (2022).
17. B. Lu *et al.*, 3D Hexagonal Arrangement of DNA Tensegrity Triangles. *ACS Nano* **15**, 16788-16793 (2021).
18. Y. P. Ohayon *et al.*, Designing higher resolution self-assembled 3D DNA crystals via strand terminus modifications. *ACS Nano* **13**, 7957-7965 (2019).
19. K. Woloszyn *et al.*, Augmented DNA Nanoarchitectures: A Structural Library of 3D Self-Assembling Tensegrity Triangle Variants. *Adv. Mater.* **34**, 2206876 (2022).
20. C. R. Simmons *et al.*, A Self-Assembled Rhombohedral DNA Crystal Scaffold with Tunable Cavity Sizes and High-Resolution Structural Detail. *Angew. Chem. Intl. Ed.* **59**, 18619-18626 (2020).
21. C. R. Simmons *et al.*, Tuning the cavity size and chirality of self-assembling 3D DNA crystals. *J. Am. Chem. Soc.* **139**, 11254-11260 (2017).
22. C. R. Simmons *et al.*, Construction and structure determination of a three-dimensional DNA crystal. *J. Am. Chem. Soc.* **138**, 10047-10054 (2016).

23. C. Zhang *et al.*, Engineering DNA Crystals toward Studying DNA–Guest Molecule Interactions. *J. Am. Chem. Soc.* **145**, 4853-4859 (2023).
24. Y. Zhao *et al.*, The Formation and Displacement of Ordered DNA Triplexes in Self-Assembled Three-Dimensional DNA Crystals. *J. Am. Chem. Soc.* **145**, 3599-3605 (2023).
25. M. Zheng, Z. Li, C. Zhang, N. C. Seeman, C. Mao, Powering≈ 50 μm Motion by a Molecular Event in DNA Crystals. *Adv. Mater.*, **34**, 2200441 (2022).
26. Z. Li *et al.*, Making engineered 3D DNA crystals robust. *J. Am. Chem. Soc.* **141**, 15850-15855 (2019).
27. C. Geng, P. J. Paukstelis, DNA crystals as vehicles for biocatalysis. *J. Am. Chem. Soc.* **136**, 7817-7820 (2014).
28. S. Vecchioni *et al.*, Metal-Mediated DNA Nanotechnology in 3D: Structural Library by Templated Diffraction. *Adv. Mater.*, **35**, 2210938 (2023).
29. S. Vecchioni *et al.*, The Rule of Thirds: Controlling Junction Chirality and Polarity in 3D DNA Tiles. *Small* **19**, 2206511 (2023).
30. J. J. Birac, W. B. Sherman, J. Kopatsch, P. E. Constantinou, N. C. Seeman, Architecture with GIDEON, a program for design in structural DNA nanotechnology. *J. Mol. Graphics Model.* **25**, 470-480 (2006).
31. D. Liu, G. Chen, U. Akhter, T. M. Cronin, Y. Weizmann, Creating complex molecular topologies by configuring DNA four-way junctions. *Nature chemistry* **8**, 907-914 (2016).
32. D. Liu *et al.*, Synthesizing topological structures containing RNA. *Nature Comm.* **8**, 14936 (2017).
33. P. S. Ho, B. F. Eichman, The crystal structures of DNA Holliday junctions. *Curr. Op. Struct. Biol.* **11**, 302-308 (2001).
34. T. Liedl, B. Högberg, J. Tytell, D. E. Ingber, W. M. Shih, Self-assembly of three-dimensional prestressed tensegrity structures from DNA. *Nature Nanotechnol.* **5**, 520-524 (2010).
35. C. Hernandez *et al.*, Self-assembly of 3D DNA crystals containing a torsionally stressed component. *Cell Chem. Biol.* **24**, 1401-1406 (2017).
36. N. Nguyen *et al.*, The absence of tertiary interactions in a self-assembled DNA crystal structure. *J. Mol. Recog.* **25**, 234-237 (2012).
37. C. R. Simmons *et al.*, The influence of Holliday junction sequence and dynamics on DNA crystal self-assembly. *Nature Comm.* **13**, 3112-3120 (2022).
38. Y. Wang, X. Guo, B. Kou, L. Zhang, S.-J. Xiao, Small circular DNA molecules as triangular scaffolds for the growth of 3D single crystals. *Biomolecules* **10**, 814 (2020).
39. C. Au, T. Woo, Ribbons: their geometry and topology. *Computer-Aided Desig App.* **1**, 1-6 (2004).
40. E. Panagiotou, The linking number in systems with periodic boundary conditions. *J. Comp. Phys.* **300**, 533-573 (2015).
41. S. Hu, M. Lundgren, A. J. Niemi, Discrete Frenet frame, inflection point solitons, and curve visualization with applications to folded proteins. *Phys. Rev. E* **83**, 061908 (2011).
42. M. Bzymek, N. H. Thayer, S. D. Oh, N. Kleckner, N. Hunter, Double Holliday junctions are intermediates of DNA break repair. *Nature* **464**, 937-941 (2010).
43. X. Wang *et al.*, Paranemic crossover DNA: there and back again. *Chem. Rev.* **119**, 6273-6289 (2018).

44. A. K. Mazur, T.-S. Nguyen, E. Gladyshev, Direct homologous dsDNA–dsDNA pairing: how, where, and why? *J. Mol. Biol.* **432**, 737-744 (2020).
45. E. Gladyshev, N. Kleckner, Recombination-independent recognition of DNA homology for repeat-induced point mutation (RIP) is modulated by the underlying nucleotide sequence. *PLoS Genetics* **12**, e1006015 (2016).
46. X. Wang, X. Zhang, C. Mao, N. C. Seeman, Double-stranded DNA homology produces a physical signature. *Proc. Natl. Acad. Sci.* **107**, 12547-12552 (2010).
47. X. Gao *et al.*, The PX motif of DNA binds specifically to Escherichia coli DNA polymerase I. *Biochem.* **58**, 575-581 (2018).
48. C. Lin *et al.*, In vivo cloning of artificial DNA nanostructures. *Proc. Natl. Acad. Sci.* **105**, 17626-17631 (2008).